Recent developments in terahertz optoelectronics/Développements récents
en optoélectronique térahertz

# Surface plasmon THz waves on gratings

Maxim Nazarov [a], Frédéric Garet [b], Damien Armand [b],
Alexander Shkurinov [a], Jean-Louis Coutaz [b,*]

[a] *Department of Physics and International Laser Center, M.V. Lomonosov Moscow State University, Moscow 119992, Russia*
[b] *IMEP-LAHC, Université de Savoie, 73376 Le Bourget du Lac cedex, France*

Available online 3 March 2008

**Abstract**

Because of their long propagation length at a metal surface in the far infrared, surface plasmons make potentially feasible the design and realization of 2D integrated terahertz systems over a metallic substrate. The coupling of a terahertz beam to the surface plasmon wave is very efficiently achieved by diffraction gratings engraved at the metal surface. In this article, we present a review of some recent works we performed in view of characterizing this coupling phenomenon. The analysis of the experimental data supplied by terahertz time-domain spectroscopy allows us to point out the main parameters that govern this diffraction process and the propagation of a surface plasmon over a flat or corrugated metal surface. ***To cite this article: M. Nazarov et al., C. R. Physique 9 (2008).***

© 2008 Académie des sciences. Published by Elsevier Masson SAS. All rights reserved.

**Résumé**

**Excitation et propriétés de propagation des plasmons de surface à la surface de réseaux de diffraction métalliques dans le domaine térahertz.** Dans le domaine spectral des ondes électromagnétiques térahertz, les plasmons de surface se propagent sur de très longues distances. Cette propriété permet d'imaginer des systèmes térahertz quasi-optiques bi-dimensionnels à la surface d'une plaque métallique. L'excitation de plasmons de surface à l'aide d'ondes incidentes planes peut être réalisée de façon efficace par un réseau de diffraction gravé sur le métal. Dans cet article, nous présentons un ensemble de travaux récents que nous avons effectués pour caractériser ce type d'excitation. L'analyse des données expérimentales obtenues par spectroscopie térahertz dans le domaine temporel nous a permis de mettre en exergue les principaux paramètres opto-géométriques qui entrent en jeu dans le couplage et dans la propagation des plasmons à la surface des réseaux et d'échantillons lisses. ***Pour citer cet article : M. Nazarov et al., C. R. Physique 9 (2008).***

© 2008 Académie des sciences. Published by Elsevier Masson SAS. All rights reserved.

*Keywords:* Terahertz; Surface plasmons

*Mots-clés :* Térahertz ; Plasmons de surface

---

* Corresponding author.
  *E-mail address:* jean-louis.coutaz@univ-savoie.fr (J.-L. Coutaz).

## 1. Introduction

Among all the numerous foreseen applications of electromagnetic waves ranging in the terahertz (THz) spectral domain, i.e. in the far infrared region, spectroscopic applications are most interesting as they allow one to monitor atmospheric pollution by molecules that are otherwise difficult to detect [1,2], to identify by spectral imagery forbidden hidden items carried by people (explosive materials, drugs, . . . ) [3,4], to detect lethal gases, and so on. Many of these applications are based on the unique spectral response of given molecules and materials in the far infrared, which does not exist in other parts of the electromagnetic spectrum, mostly in the visible and in the infrared. For example [5], it is well know that hydrogen sulfide ($H_2S$), of outstanding importance in the environment, is difficult to be detected in the visible or infrared ranges because of the lake of strong absorption lines. On the other hand, $H_2S$ exhibits a typical signature in the THz frequency range, originating in the excitation of rotation energy levels.

In modern spectroscopy, surface studies are performed by numerous laboratories, because they reveal phenomena that are not only relevant from the academic point of view but also in actual life, as they can explain oxidation and catalysis effects, diffusion of species through membranes, . . . . Also, surface electromagnetic effects could enhance the efficiency of numerous physical and chemical processes [6], as these effects lead to an increase of the electromagnetic fields at the surface, giving rise to an improved experimental sensitivity. In particular, the excitation of surface plasmons (SP) [7] at the metal surface may increase by three orders of magnitude the intensity of optical beams generated at the surface, like Raman or second harmonic signals [8].

Thus, performing surface spectroscopy in the far infrared would lead to fruitful results. In addition, since the beginning of the 1990s, huge THz systems are competing with more compact and versatile set-ups, mostly based on optoelectronic techniques, which have permitted THz spectroscopy to spread to many laboratories worldwide. For example, THz time-domain spectroscopy (THz-TDS) is nowadays a mature technique [9,10] that exhibits an amazing performance (unrivaled bandwidth from 0.1 THz up to 5–6 THz, large dynamic range, high temporal resolution and measurement of both amplitude and phase of the signals). Moreover, the combination of THz-TDS techniques and surface wave excitation is expected to give valuable scientific results, as surface waves exhibit remarkable properties in the far infrared. For example, THz SP propagate over very long distances, leading either to a strong field enhancement at metal surfaces, or to the possibility of using THz SP as a means of signal transmission on a 2D metal surface. In addition, THz SP are so robust that they can propagate over a discontinuous periodic metal surface [11,12], i.e. a 2D grid, and they can jump from one metal edge to another [13].

In this article, we give a review of the preliminary recent works we performed with the aim of building a surface THz-TDS system using SP as the signal carrier and as a mean to enhance the interaction between the electromagnetic field and the surface. The SP excitation with a parallel incoming beam can be achieved using a prism coupler [14], a grating coupler [15], or an edge located over the surface [16]. If permitted by the device geometry, coupling at the end of the surface is also possible. To fabricate user-friendly systems, we think that grating structures are the most pertinent, as they show many advantages over other coupling structures: well-controlled coupling, easy and reproducible fabrication using common lithography, etching, and mechanical processes, quasi two-dimensional devices. Most of the works reported here concern both the excitation of SP with a metallic grating coupler and the propagation properties of SPs at a metal surface.

## 2. Theoretical basis

### 2.1. SP and guided modes in the THz range

SP describe electromagnetic waves propagating at the interface between two media, one of them being a dielectric (the inactive medium), the other one containing free carriers (the active medium) in such a way that the product of the dielectric constants of the two media is negative [7]. For sake of simplicity, we suppose from now on that the inactive medium is air and the active medium is a metal (or a doped semiconductor). A SP corresponds to the quantum of energy associated to a harmonic oscillation of the free charges at the metal surface (the SP wave), which is mostly perpendicular to the surface and which propagates along the surface. Solving Maxwell equations (homogeneous problem) for this interface leads to the SP dispersion relation:

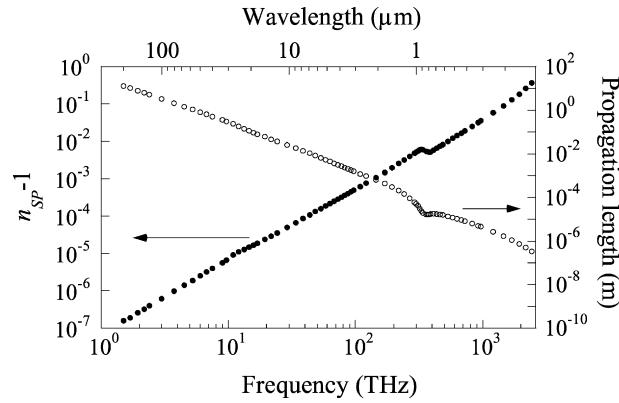$$k_{SP} = \frac{\omega}{c} \sqrt{\frac{\varepsilon}{1+\varepsilon}} \qquad (1)$$

Fig. 1. Calculated values of the difference $n_{SP} - n_{air}$ and of the SP propagation length LSP for a surface plasmon propagating over a flat aluminum surface. The dielectric constant of aluminum required for performing the calculation is taken from [17].

where $\varepsilon = \varepsilon_r + j\varepsilon_i$ is the dielectric constant of the metal. In the far infrared, this dielectric constant takes large values, thus:

$$k_{SP} \approx \frac{\omega}{c}\left(1 - \frac{1}{2\varepsilon}\right) \tag{2}$$

Moreover, the dielectric constant obeys well the Drude model [17]:

$$\varepsilon = \varepsilon_\infty - \frac{\omega_p^2}{\omega(\omega + j\Gamma)} \approx -\frac{\omega_p^2}{\omega(\omega + j\Gamma)} \tag{3}$$

$\omega_p^2 = Ne^2/(m_e\varepsilon_o)$ is the metal plasma angular frequency, $\varepsilon_\infty$ is the dielectric constant at higher frequencies, $N$, $e$ and $m_e$ are respectively the electron density, charge and effective mass, and $\Gamma$ is a damping pulsation that accounts for a finite conductivity of the metal. Introducing the Drude expression in (2) leads to:

$$n_{SP} \approx 1 + \frac{\omega^2}{2\omega_p^2} + j\frac{\omega}{2\omega_p^2}\Gamma \tag{4}$$

where $n_{SP}$ is the complex SP effective index. As expected for a guided wave, the real part of $n_{SP}$ is larger than $n_{air} = 1$; nevertheless, the difference is extremely weak as the plasma frequency lies within the UV region for most metals [18]. Thus $\omega_p/\omega = 1000$–$3000$ in the far infrared and $n_{SP} - n_{air} = 5 \times 10^{-6} \sim 5 \times 10^{-7}$. On the other hand, SP experiences weak propagation attenuation in the far infrared. The attenuation coefficient can be written:

$$\alpha_{SP} = 2\frac{\omega}{c}\,\mathrm{Imag}(n_{SP}) \approx \frac{\omega^2}{\omega_p^2}\frac{\Gamma}{c} \tag{5}$$

The damping pulsation $\Gamma$ ranges within 3–20 THz [18], leading to a propagation length $L_{SP} = \alpha_{SP}^{-1}$ of several meters. This is due to the fact that the SP field is mainly located in air and not in the metal. The decay length $d_{air}$ of the THz SP field in air is:

$$d_{air} \approx \frac{2c\omega_p}{\sqrt{2\Gamma\omega_p^3}} \tag{6}$$

For SP in the THz range, $d_{air}$ is of the order of cm. Fig. 1 shows the calculated values of $n_{SP}$ and $L_{SP}$ over the spectral range from THz to UV, using data for aluminum collected by Rakic [17]. At THz frequencies, $n_{SP}$ differs from 1 by less than $10^{-6}$, i.e. less than 0.002% of the SP energy is located in the metal. Accordingly, the propagation length reaches several meters, $10^6$ more than in the visible range.

## 2.2. The grating coupler

A guided wave, either a SP at a metal surface or a wave guided in a dielectric slab, shows a wavevector component along the guiding direction larger than the wavevector of a plane wave propagating in the surrounding media. This

makes certain the location of the guided energy inside the waveguide or in its close vicinity, with an evanescent tail in the surrounding media. A grating engraved at the waveguide surface permits to one couple an incident plane wave to a guided mode by matching their wavevectors. Indeed, as the grating is a periodic structure, the conservation laws for the electromagnetic field at the grating surface lead to the well-known diffraction equation:

$$k_i + m\frac{2\pi}{\Lambda} = k_m \tag{7}$$

where $k_i$ and $k_m$ are the components parallel to the device surface of the incident and diffracted wavevectors, respectively, $\Lambda$ is the grating period and $m$ is an integer. At first glance, when the grating acts only as a weak perturbation, the incoming light is coupled to a guided mode when:

$$k_m = k_{\text{guided}} \tag{8}$$

where $k_{\text{guided}}$ is the wavevector of the guided mode.

A more detailed analysis reveals that the incoming light beam is partly reflected, transmitted and coupled into the waveguide. Let us use here the coupled mode theory [19] written for the grating coupler [20], which is well adapted to treat the excitation by limited beams. The amplitude $A_{\text{gw}}(x)$ of a monochromatic guided wave, where $x$ is the direction along the surface, obeys the following differential equation:

$$\frac{\partial A_{\text{gw}}(x)}{\partial x} - j(k_p - k_m)A_{\text{gw}}(x) = jt_p A_i(x) \tag{9}$$

$k_p$ is the wavevector along $x$ associated to the mode $p$ of the structure ($k_p$ is complex even in lossless structures because the mode is leaky) and $t_p$ is the coupling coefficient related to $k_p$ ($t_p$ is determined numerically using a plane wave analysis). $A_i(x)$ is the profile of the incident amplitude along $x$ at the grating surface. The field amplitude $F_n(x, z = 0)$ of a diffracted order labeled $n$ at the grating surface ($z = 0$) is given by:

$$F_n(x, z = 0) = d_n\left[A_i(x) + \frac{k_p - k_{z,n}}{t_p}A_{\text{gw}}(x)\right] \tag{10}$$

$d_n$ is the factor independent of the angle of incidence (in the vicinity of the resonance angle) but depending on the grating groove depth $h$, and $k_{z,n}$ is the zero of the radiated order $n$. The far field amplitude of the diffracted order is obtained by a Fourier transform of relation (10). It is known that $\Re(k_{z,n}) \approx \Re(k_p)$, where $\Re(\cdot)$ denotes the real part. Moreover, at resonance, $k_m = \Re(k_p)$, thus:

$$\begin{cases} \dfrac{\partial A_{\text{gw}}(x)}{\partial x} + k_p'' A_{\text{gw}}(x) = jt_p A_i(x) \\ F_n(x, y = 0) = d_n\left[A_i(x) + j\dfrac{k_p'' - k_{z,n}''}{t_p}A_{\text{gw}}(x)\right] \end{cases} \tag{11}$$

where the superscript $''$ indicates the imaginary part of the value. These two equations show that the guided wave amplitude is fed by the incident amplitude and it varies along $x$ due to both excitation and loss of energy through diffraction. The diffracted amplitude is the sum of the reflected field and the part of the guided wave that is diffracted. The system (11) may be solved for different shapes of the incident beam, such as rectangular or Gaussian excitations [20]. Performing the Fourier transform of (10) gives the far field dependence of the diffracted field versus frequency for a given angle of observation $\theta$:

$$F_n(\theta) \propto d_n A_i(\theta)\frac{k_m - k_{z,n}}{k_m - k_p} \tag{12}$$

Depending on the position of the zero in the complex plane, the far field pattern could exhibit a black or a bright line at resonance when the angular width of the incident beam is larger than the width of the resonance. In the case of SP, only dark lines are observed. From (12), it is easy to show that at optimization (that is for $F_n(\theta_{\text{res}}) = 0$) the absorption coefficient $\alpha_p$ of the guided mode $p$ is related to the frequency width of the dark line:

$$\frac{\Delta\omega}{c}\sin\theta = 2k_p'' \quad \Rightarrow \quad \alpha_p = \frac{\Delta\omega}{c}\sin\theta \tag{13}$$

Thus analyzing the far field diffraction pattern of the grating coupler allows one to determine both the effective index $n_p^{\text{eff}}$ of the guided mode $p$ ($k_m = \Re(k_p) = \frac{\omega}{c}n_p^{\text{eff}}$) and its absorption coefficient $\alpha_p$.

Table 1
Parameters of the gratings used in this work

| Sample | Material | Groove shape | Period $\Lambda$ (mm) | Groove depth $h$ ($\mu$m) | Filling factor (%) |
|---|---|---|---|---|---|
| A | duralumin | rectangular | 1.6 | 90 | 38 |
| B | duralumin | rectangular | 1.6 | 110 | 48 |
| C | duralumin | rectangular | 1.2 | 73 | 53 |
| D | aluminum | triangular | 0.3 | 75 | 50 |
| F | aluminum | triangular | 0.375 | 375 | 50 |
| G | aluminum | sinusoidal | 0.75 | 74 | 50 |

For designing grating structures and for modeling the experimental data, we use a rigorous diffraction theory, namely the integral method [21] for metallic grating diffraction. The method is based on a Green function formalism, in which the incident beam creates a current density at the grating surface which acts a localized source for the diffracted signal.

## 3. Experiments

### 3.1. Samples

We use different types of gratings (see Table 1) engraved at a metal surface to study the excitation and propagation of SP in the THz range.

Metallic grating with a rectangular groove shape were made from a flat 1-cm thick duralumin sheet ($\sim$94% aluminum, $\sim$5% copper and a small amount of magnesium and manganese) on which the diffraction grating is manufactured using a milling machine [22] (hereafter, those samples are labeled A, B and C). For the different samples used in this study, the grating periodicity $\Lambda$ varies in the range 0.6–1.6 mm, the grooves are almost rectangular with a filling factor (ratio of upper part length to the period) taking values from 30 to 70%, and the groove depth $h$ ranges from 70 to 130 $\mu$m. When using the grating as a coupler to study the SP propagation properties on a flat metal surface (duralumin), the grating area ($1.5 \times 2.5$ cm$^2$) is located 3 cm from the duralumin sheet edge. This edge corresponds to the intersection of the flat horizontal and vertical sides of the sheet, which form a $\pi/2$ angle. We use two devices for exciting SP and then diffracting the SP towards a detector. Both emitting and receiving gratings are similar except that the emitter (A) groove depth is smaller to reduce diffraction losses of SP propagating along the grating, while the detector (B) groove depth is larger to get a good outcoupling efficiency. Triangular-shaped grating (D and F) where fabricated in the same way. The groove shape is sawtooth-like with a right angle profile, corresponding to a blaze angle in the THz range of 15°. The grating length is $l_D = 8$ cm.

Sine-shaped gratings (G) were manufactured by stamping a 100-$\mu$m thick aluminum foil stick on a thick PMMA substrate. Sample G [23] consists of two diffraction gratings $A_G$ and $B_G$ connected by a flat surface region between them. The gratings of the G sample have a sine profile with a groove period of $\Lambda = 0.75$ mm and the groove depth $h = 74$ $\mu$m. The G grating length is $l_G = 33$ mm. The size of the THz beam on the grating surface roughly corresponds to the grating size (at the incidence angle $\theta = 34°$). Additional third grating $C_G$ was added on G for the propagation losses experiments.

### 3.2. Set-ups

The experiments are performed using a classical THz time-domain set-up that was already described in Refs. [22,24,25]. The THz beam is p-polarized (transverse magnetic) and its spectrum spreads up to 4 THz. Nevertheless, due to loss of energy by diffraction, the useful detected signal is limited to 1.5 THz. Both detector and emitter are photoconductive antennas for experiments with gratings A, B and C, and non-linear crystals for experiments with gratings D and G. The THz beam delivered by photoconductive antennas is made parallel by a large aperture silicon lens: at the device location, the THz beam diameter is $\phi = 1.5$ cm at 0.5 THz, with an angular divergence smaller than 3°. The THz detector position could be adjusted to record the signal reflected by the grating, or diffracted by
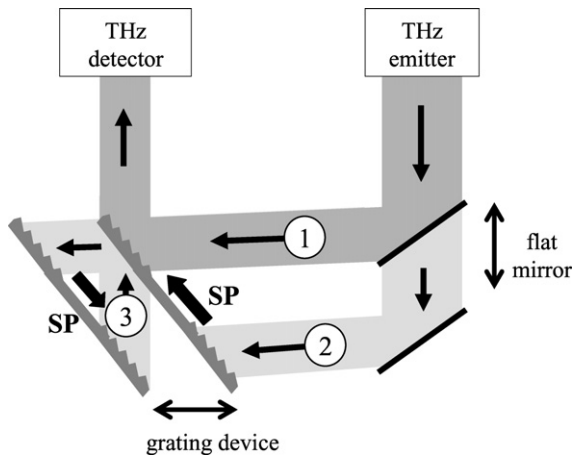
Fig. 2. SP excitation and propagation schemes: (1) specular reflection, (2) forward propagation and (3) backward propagation.
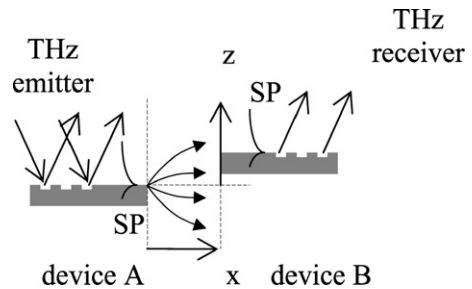
Fig. 3. SP jump between two metallic sheets.

a second device in the SP propagation experiment (Fig. 2). In both cases, the signals are focused onto the THz detector by a second large aperture silicon lens. The second device can be moved in directions $x$ and $z$ (Fig. 3) using micrometer translation stages. To get broader spectra (up to 3 THz) and larger beam cross-section (25 mm) we use another similar set-up with ZnTe crystals as emitter and detector, parabolic mirrors for the collimation and focusing of the THz beam [23].

To study the SP propagation properties, the THz beam is shifted in a direction parallel to the grating surface (see Fig. 2) to excite the SP in various grating areas; angles of incidence and angles of the output radiation were preserved while moving the THz beam along the sample surface. By a parallel movement of a flat mirror, we also shift the SP excitation area relative to the area of SP detection. To change the incidence angle, we move and rotate the grating sample and we adjust the flat mirror position and angle. A slit diaphragm in THz beam is used to study beam size role and to determine the SP amplitude in a particular point on the grating.

## 4. Results

### 4.1. Short THz pulse diffraction

The simplest interaction of radiation with the metal grating is diffraction. We first study peculiarities of single-cycle pulse diffraction in time and frequency domain. For non-specular reflection from grating samples, we analyze changes in pulse duration and frequency bandwidth depending on incidence angle, grating period and blaze angle. In the time domain, any diffracted ultrashort terahertz pulse expands in both directions of time, has symmetrical smooth envelope shape (see Fig. 4) and linear phase spectrum. In the frequency domain and for given incident and observation directions, we get several narrowband maxima $f_m$ (harmonics: $f_m/m$ is almost constant as derived from (7)) (see Fig. 5).

Fig. 6 presents an enlarged view around 0.8 THz of the spectrum shown in Fig. 5, as well as the phase of the signal. To get rid of the strong variation of the phase with frequency, we plot the equivalent thickness $L_\phi$, which is related to the phase $\phi$ by: $\phi = \frac{2\pi f}{c} L_\phi$. This allows us to observe small variations of the curve that are usually hidden by the strong slope. We see that $L_\phi$ is almost constant within the resonance (let us remember that at 0.8 THz, the wavelength $\lambda = 0.375$ mm). The bandwidth of each peak seen in Fig. 5 is determined by beam size and detector aperture. For all the collection of gratings studied here, we measure a maximal diffraction efficiency of the order of 30%. The possibility of an easy control of the wide spectrum of terahertz radiation pulse is thus demonstrated. Terahertz pulse diffraction can be described by the laws of classic diffraction optics, despite the fact that at particular moment of time only several grating periods are illuminated by the short THz pulse.
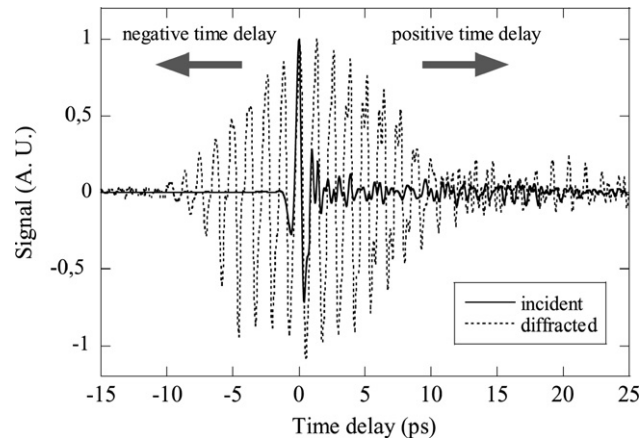
Fig. 4. THz pulse waveforms: incident (continuous line) and reflected (dashed line) by grating D. The signals are normalized to 1 and have been shifted in time to be centered around $t = 0$. The angles of incidence and of the diffraction beam are 55° and 35°, respectively.
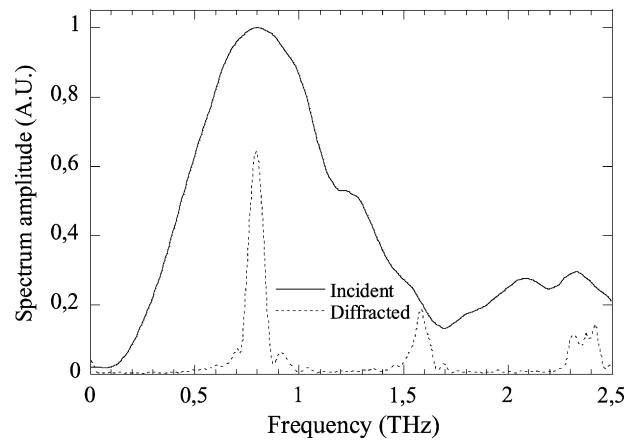


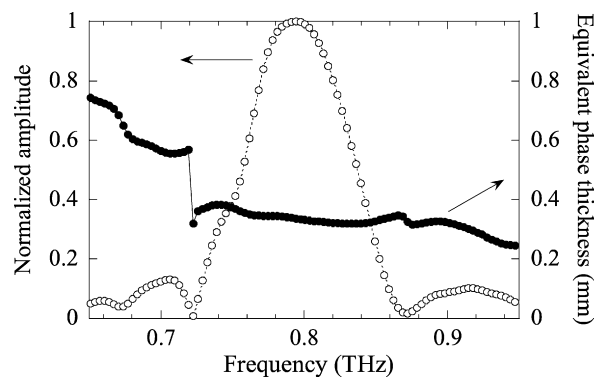Fig. 5. Spectra of the incident and diffracted THz pulse waveforms shown in Fig. 4.



Fig. 6. Zoom around 0.8 THz of the diffracted signal shown in Fig. 5. Open circles: diffracted amplitude. Full circles: spectrum of the phase presented in terms of equivalent propagation thickness $L_\phi$.

## 4.2. SP excitation and optimization of the excitation efficiency

Very similar temporal and spectra transformations are observed when SP are excited, but the influence of guided mode excitation and short pulses propagation is clearly seen (see Fig. 7, grating D). The presence of sharp dark lines
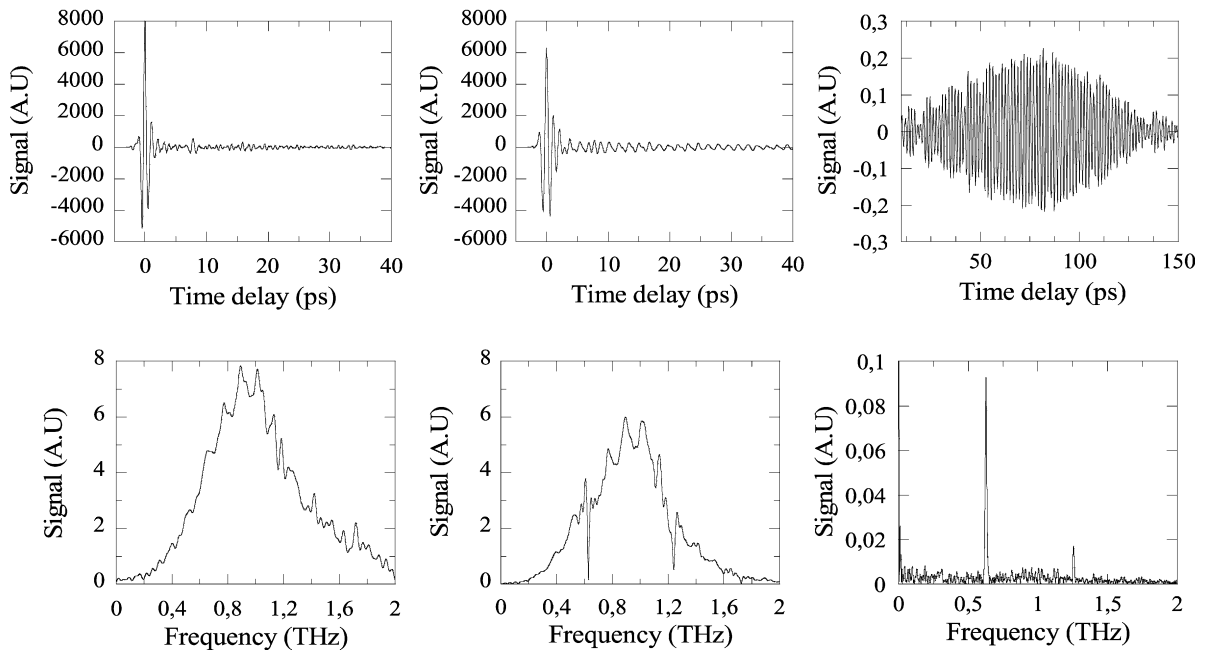
Fig. 7. Time waveforms of the incident THz pulse (as reflected by a flat aluminum mirror), of the pulse reflected by grating D and of the pulse diffracted towards the detector by a distant area of the grating D (upper row); corresponding spectra (lower row).
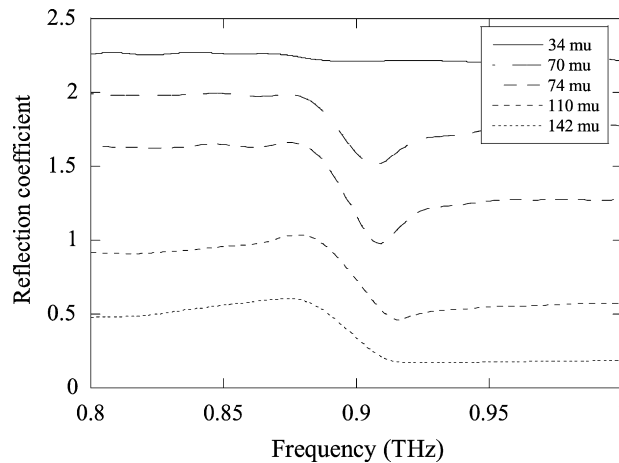


Fig. 8. Zoom around 0.9 THz of the experimental THz spectra reflected by aluminum gratings (period $\Lambda = 750$ μm) of sinusoidal groove shapes with different groove heights indicated in the inset. For sake of legibility, each plot is shift vertically by 0.4 as compared to the one below.

in the reflected spectrum leads to long oscillations in the temporal signal. On the other hand, the signal diffracted by a distant area of the grating D, i.e. by a part of the grating far from the illuminated region, is proportional to the energy coupled to the SP and it shows an oscillatory temporal behavior. The spectrum reveals two narrow peaks at 0.63 and 1.2 THz respectively. They correspond to the excitation of a SP through diffraction orders $m = -1$ and $m = -2$ respectively. This confirms that energy missing in the reflected spectrum around 0.63 THz is coupled to the SP wave. The signal diffracted by a distant area of the grating D is radiated in the same specular direction than the reflected signal, because similar phase-matching is fulfilled for in- and out-coupling.

Fig. 8 shows experimental spectra of the coefficient of reflection of gratings with sinusoidal groove shape (period $\Lambda = 750$ μm) and different groove depths. The dip observed close to 0.9 THz corresponds to the excitation of a SP propagating in the forward direction through the diffracted order $m = +1$. As expected, the effective index of the SP
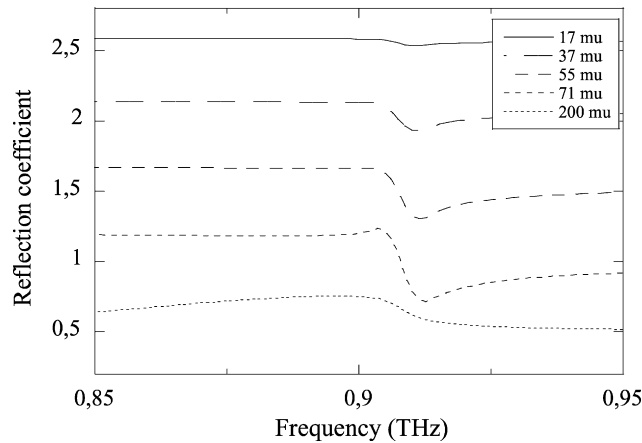
Fig. 9. Calculated THz spectra reflected by aluminum gratings (period $\Lambda = 750$ μm) of sinusoidal groove shapes with different groove heights indicated in the inset. For sake of legibility, each plot is shift vertically by 0.4 as compared to the one below.

is extremely close to 1. As explained above, the groove depth serves as a coupling constant which controls the shape of the $m$-line, in particular the minimum of the dip and thus the coupling efficiency. As seen in Fig. 8, there exists an optimum groove depth (here $h_{\mathrm{opt}} = 74$ μm, i.e. $\sim \Lambda/10$) for which the coupling efficiency is maximum. Fig. 9 shows the corresponding calculated curves. The general shapes of the calculated curves are comparable to the measured ones, and the coupling efficiency optimization is clearly observed. Differences with the measured data, especially the spectral width of the resonance, arise certainly from the actual groove shape, which is not perfectly sinusoidal. Oxidation or chemical contamination at the metallic grating surface may lead to additional losses that could also explain the difference between calculated and measured curves, especially the much broader experimental resonance width.

### 4.3. SP coupling dispersion and Bragg effect

When the broadband THz pulse is incident on the grating surface at the angle $\theta$, only given frequencies $f_m$ obeying the phase matching condition (7) can be transformed into SP, where $m$ is a diffraction order. We determine the SP effective index by recording and analyzing the experimental $f_m$ values for which dips are observed in the reflected spectrum.

In this determination, the first step consists in attributing to each experimental dip the related order of diffraction $m$, as well as the direction of the SP propagation (+ for co-propagation, i.e. SP propagating along $x$ in the direction of $k_i$, − for contra-propagation). Fig. 10 represents the whole spectrum of the coefficient of reflection of a rectangular shape grating B, with $\Lambda = 1.6$ mm, $\theta = 35°$ and $h = 120$ μm. Several dips are observed. Using relation (7) and $n_{\mathrm{eff}} \sim 1$, the diffracted order $m$ involved in the coupling process as well as the direction of propagation of the excited SP are determined and given in the figure. The strongest coupling is observed for the co-propagation SP excitation. For contra-propagative SP, excitation through orders with $m$ as high as 5 is observed.

From the experimental value of $n_{\mathrm{eff}}$ and using (4), it should be possible to derive the dielectric constant $\varepsilon$ of aluminum. However, due to the huge epsilon value of metals in the THz range, the experimental values lead to $n_{\mathrm{eff}} \sim 1$ ($\pm 0.02$), without enough accuracy to determine $\varepsilon$.

Fig. 11 shows the dispersion of the SP coupling, i.e. the frequency $f_m$ of a $m$-line for which a SP is excited versus the angle of incidence (recorded using grating C). The lines are calculated using (7) and $n_{\mathrm{eff}} \sim 1$.

At the Bragg frequency, SP are excited both in the forward and backward directions through 2 different diffraction orders, let us say $m$ and $p$. This occurs when:

$$k_i + m\frac{2\pi}{\Lambda} = k_{\mathrm{SP}} \quad \text{and} \quad k_i + p\frac{2\pi}{\Lambda} = -k_{\mathrm{SP}} \quad \Rightarrow \quad f_{\mathrm{Bragg}} = (m - p)\frac{c}{2n_{\mathrm{eff}}\Lambda}$$

This is observed when two dispersion lines intersect, as seen on Fig. 11 for $\theta = 30.2°$ and $f \sim 0.495$ THz for the curves $m = +1$ and $p = -3$. The two contra-propagating SP produce a standing surface wave, leading to a forbidden
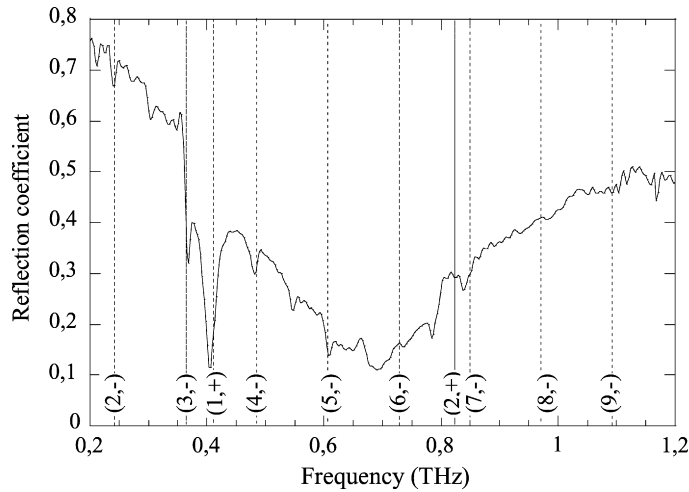
Fig. 10. Spectrum of the coefficient of reflection of a grating with rectangular-shaped grooves ($\Lambda = 1.6$ mm) for $\theta = 33°$. The vertical dashed lines indicate the position of the phase-matched frequencies $f_m$. The numbers correspond to the order of diffraction involved in the coupling, the sign $+(-)$ is for co(contra)-propagative excited SP.
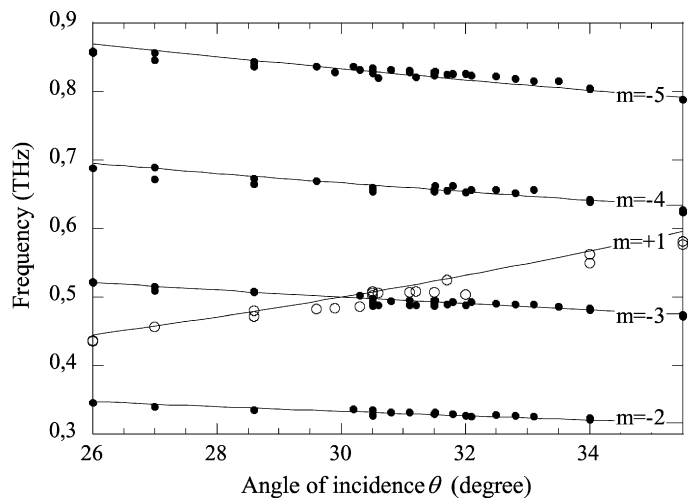


Fig. 11. Dispersion of the SP coupling process, i.e. coupled SP frequency versus the angle of incidence. Circles are experimental data obtained with grating C. The lines are calculated using (4) with $n_{\text{eff}} \sim 1$.

bandgap in the dispersion curves. The net result is a repelling of the two dispersion curves in the vicinity of a Bragg frequency. The forbidden bandgap can be difficult to observe and to measure with a good precision in a reflection experiment. Indeed, the coupling strength can be more efficient for one SP than for the second one. Thus its related $m$-line is darker than the second one which is hidden by the first one.

Here we propose an original method to measure the bandgap with a great accuracy. We use a second grating engraved besides the first grating on the same metal sheet to couple out the SP energy towards the detector. Thus the signal from a SP is not perturbated by the other propagating in the opposite direction, even if this signal is much weaker. The relative position of this second grating with regards to the first one allows us to detect either the co- or the contra-propagating SP. Fig. 12 shows the recorded frequency bandgap for grating A, as well as the calculated dispersion curves that fit nicely the experimental data. The bandgap width is 20 GHz.
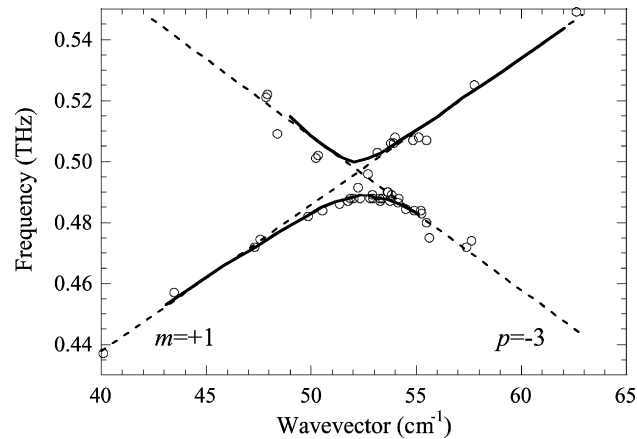
Fig. 12. Accurate record of the frequency bandgap due to the Bragg effect. Open circles are values measured with grating C, the continuous lines are calculated using the integral method, and the dashed lines are only a guide to the eye, indicating which order of diffraction is involved in the SP coupling phenomenon.

### 4.4. SP spectral bandwidth

The SP bandwidth is mainly determined by incident beam parameters – angular divergence and cross-section size [22,23]. The last one can be transformed into number of illuminated grooves. It is interesting to recall that grooves are illuminated one after one in time because of short pulse duration and oblique incidence. For not optimized grating shape (too high $h$), bandwidth may be increased due to considerable diffraction losses on each groove.

With large slits in front of the sample (D grating) and of the detector (slit widths $L_1 = L_2 = 15$ mm), we observed the longest SP duration whose Fourier spectrum width is 9 GHz (FWHM). With smaller slits ($L_1 = L_2 = 7$ mm), the pulse duration is reduced and the spectrum width increases proportionally up to 12 GHz. Thus geometrical sizes influence the measured TSP bandwidth. Note that the expected metal losses are almost negligible and would have lead, for an optimized configuration and an ideal plane wave excitation, to a SP bandwidth narrower than the frequency resolution of the set-up (6 GHz).

### 4.5. Propagation losses and coupling efficiency of SP

The energy coupled to the SP is diffracted by the grating while SP propagates along the grating surface. This diffracted signal contributes to a part of the ripples observed after the main reflected signal in the temporal waveform (Figs. 4 and 7). To evaluate the amount of this diffracted SP energy, we perform another experiment [23] with device G, in which grating $A_G$ is used to excite the SP while grating $B_G$ allows us to measure the SP signal transmitted by the flat surface in between $A_G$ and $B_G$. In the last stage, a third similar grating $C_G$ was located in between the two others ($A_G$ and $B_G$), all of them being engraved on the same aluminum substrate: measuring the signal diffracted by $B_G$ leads to determining the transmission of SP energy through $C_G$. The so-measured diffraction losses of grating $C_G$ is about 50%, which means that half the incoming SP energy is diffracted in free space by grating $C_G$. By comparing $A_G$–$B_G$, $A_G$–$C_G$ and $B_G$–$C_G$ transition efficiencies, we obtain the SP propagation length over the flat aluminum surface, namely 10 cm (Fig. 13).

When SP propagates over a long grating, we can trace its amplitude by measuring the outcoupled radiation at local distant points [23]. The so-measured SP propagation length on the grating is 2 cm (Fig. 13). Losses are larger than for propagation over a flat surface, because a part of the SP energy is diffracted out by the grating. We also estimated [22] the SP coupling efficiency and losses by comparing incident energy, reflected energy and energy of the propagating SP outcoupled at different locations over the grating. Energy was evaluated only in the SP narrow frequency band. For optimized gratings, we obtained about 50% energy transformation to narrowband SP.

To get rid of the coupling efficiency problem, we performed a complementary experiment in which an additional 2 cm-thick bar of duralumin was inserted in between the two devices, making 8-cm long the total SP propagation length between the two gratings, and we compared the results with the 6-cm propagation case. We obtain propagation
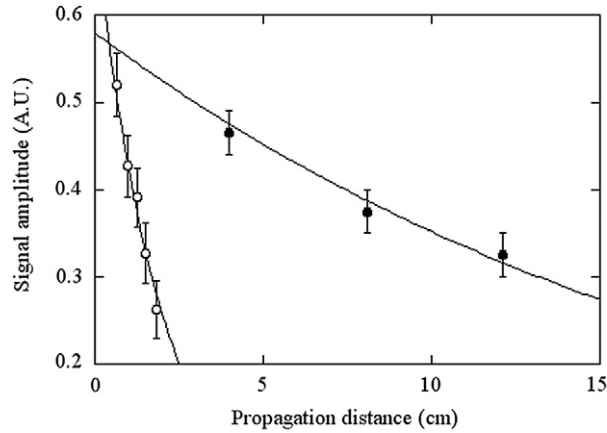
Fig. 13.

attenuation $\alpha = 0.048$ cm$^{-1}$ on a flat metal surface, a value that is comparable with $\alpha = 0.023$ cm$^{-1}$ reported by Jeon and Grischkowsky [26].

### 4.6. SP dynamics

The SP lifetime $\tau$ is related to its propagation length $L$ over a flat surface. As the SP amplitude suffers attenuation versus the propagation distance $x$, see relation (11), we can write:

$$A_{SP}(x,t) \propto e^{-x/L} e^{j\omega t}$$

However, $x = v_{SP}t$ where $v_{SP}$ is the SP phase velocity. Thus we obtain:

$$A_{SP}(x,t) \propto e^{-t/\tau} e^{j\omega t}$$

with $\tau = L/v_{SP}$. On the other hand, the duration of SP signal is due the excitation over an oblique incidence of the SP at different locations of the grating coupler by the incoming THz pulse. Therefore, in contrast with simple diffraction on a grating, the duration of the detected pulse depends on SP propagation relative to incidence direction. For example, with C grating and $\theta = 34°$, SP duration radiated after propagation 'forward' at $f = 0.55$ THz is 50% smaller than SP duration radiated after propagation 'backward' at $f = 0.48$ THz. Here SP at $m = +1$ and $m = -3$ are excited and detected with the same beam size and detector aperture, and these frequencies are close to each other and are not in the band gap range (see below). In addition, in the far infrared, SP propagation length exceeds the incoming beam size and the THz pulse is much shorter than SP lifetime. Therefore SP lifetime is not equal to SP pulse duration [23].

SP is not stationary [27] over the time scale of our measurements (50 ps). For instance (see Fig. 7), we distinguish in specular reflection the periods of SP excitation (1 ∼ 3 ps) and then SP re-radiation (3 ∼ 40 ps). As explained above, remember that the SP re-radiation characteristic time depends on the area illuminated and on the detector aperture, because the amplitude decreases mainly due to SP propagation [23]. Thus we can perform a time-windowing of the experimental waveform before going to the frequency domain through a Fourier transform, in order to separate the different regimes of SP excitation and re-radiation. By shifting step by step the time-window along the temporal waveform (Fig. 14) and then performing a Fourier transform, we obtain a 2D plot that describes the coupling process dynamics (Fig. 15). The 2D plot shows the signal versus frequency and window time-delay (Wigner representation). At early times, most of the incoming spectrum is reflected by the device, but energy is missing for frequencies obeying the coupling equation (7). Conversely, at later times, energy is observed only for those frequencies: it corresponds to the energy of the propagating SP that is progressively coupled out through diffraction by the grating.

As an example, Fig. 16 shows the spectrum reflected by grating A as well as the spectrum of time-windowed ripples following the reflected pulse. The latter is attributed to the SP re-radiation and one sees that it occurs for SP excitation frequencies for which dark lines are observed in reflection.

To get a definitive proof of this hypothesis, we put the grating device B in contact with device A. Thus the SP excited at grating A propagates towards grating B where it is diffracted towards the detector. The signal detected at
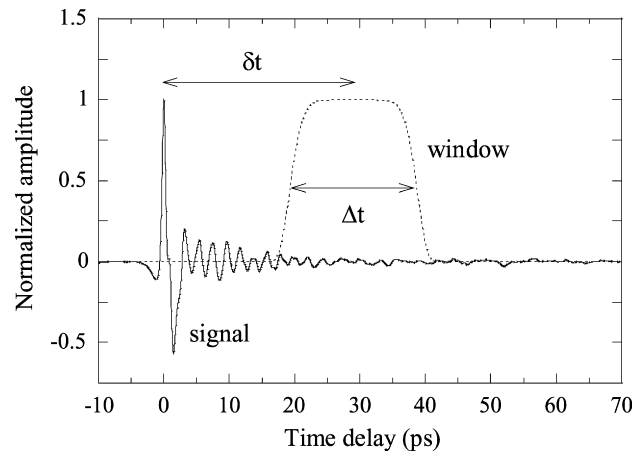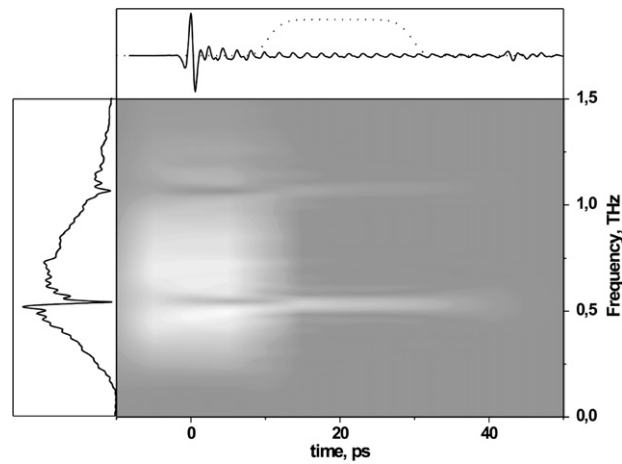
Fig. 14. The principle of the time-windowing method.

Fig. 15. Spectro-chronogram (Wigner representation) of SP excitation and radiation. The *x* scale is the time position of the temporal window, the *y* scale is the spectrum of the time-windowed signal. White parts correspond to the most intense signals.
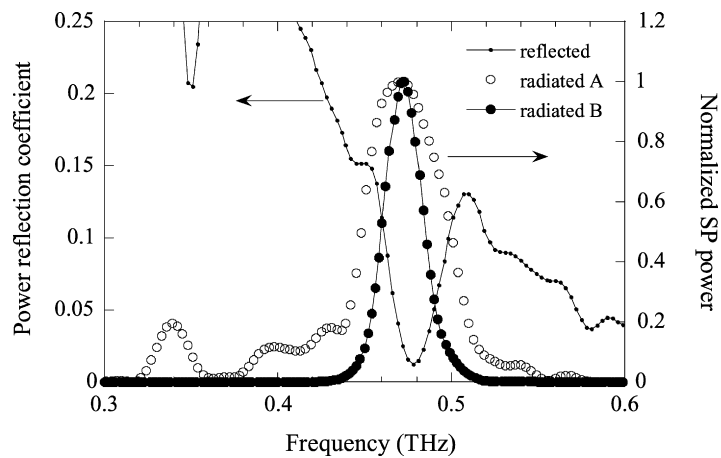
Fig. 16. Spectra of the whole temporal signal (continuous line and dots) and of the time-windowed signal (open circles) reflected by grating A, and of the signal detected at grating B (continuous line and full circles).
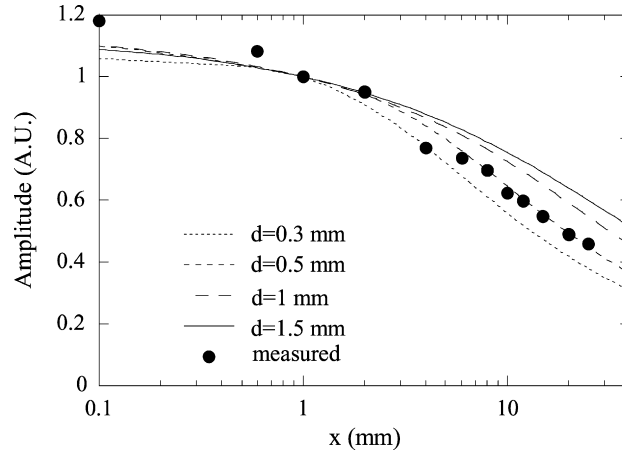
Fig. 17. SP plasmon at 0.475 THz excited at device A and detected at device B versus the distance $x$ between the two devices. The lines are calculated using a simple scalar Huygens model with the decay length $d_{air}$ of the SP in air as single adjustable parameter.

B is at the same frequency position as the signals from the ripples and the dark line in reflection, demonstrating our hypothesis. The peak at 0.475 THz recorded at device B is narrower (26 GHz FMHW) than the same peak recorded in reflection of device A (39 GHz) (Fig. 16). This is consequence of a SP ringing decay time at device A (12 ps) shorter than the SP signal at device B (29 ps (FWHM)). This can be understood, in the time-domain, as follows: the signal radiated by grating B starts to grow when the SP pulse reaches the first border of grating B, and it ends up when the last part of the SP pulse reaches the second border of grating B. As both grating are equal in size, the detected signal should be roughly twice longer than the coupled one, as observed.

*4.7. SP jump*

In a last experiment, we investigate the properties of the field radiated at the metal edge [22] by measuring the amplitude of the signal coupled to the second device versus the distance $x$ between the two devices (see Fig. 3). The two devices are set at the same elevation ($z = 0$). For each distance $x$, we record the waveform of the signal diffracted by the second device (Fig. 3) and we plot the peak value (at 0.475 THz) of its spectrum versus $x$ (Fig. 16). The experimental data, normalized at 1 for $x = 1$ mm, are presented on Fig. 17 for $x$ varying from 0.1 mm up to 25 mm, i.e. from $0.17 \times \lambda$ to $41 \times \lambda$. Thus the near field regime ($x$ smaller than a few wavelengths) as well as the far field regime ($x > 10 \times \lambda$) are studied.

As expected, the signal decreases with $x$ but the coupling efficiency remains high since 30% of the energy is coupled for $x = 10$ mm. The log plot shows a linear behavior in the far field (i.e. for $x > 6$ mm $\sim 9 \times \lambda$) while it saturates for small values of $x$. In the far field, the signal varies as $1.72x^{-0.42} \approx 1/\sqrt{x}$, which is the expected behavior of a spherical wave radiated in the far field by a dipolar or punctual source. We use a simple Huygens scalar model to fit the experimental data. We assume that the incoming SP field $E_{SP}(x = 0, z)$ is exponentially decreasing in air ($E(0, z) \propto \exp(-z/d_{air})$, $d_{air}$ is the decay length of SP in air (6)) and is almost negligible in metal because of the large dielectric constant of the metal. Each point along $z$ in the $x = 0$ plane serves as a point-source that radiates in free space a spherical wave whose weight is proportional to the amplitude $E_{SP}(x = 0, z)$ of the incoming SP field in $z$. Then we calculate the radiated field $E_{rad}(x \neq 0, z)$ at any location ($x \neq 0, z$) in free space by adding all the contributions of the points of the $x = 0$ plane. This gives us the radiated field map in a plane $x \neq 0$. Finally, we define the coupling efficiency $\eta(x)$ as the overlapping integral of the radiated field and the TSP field at the second device:

$$\eta(x) \propto \int_{-\infty}^{+\infty} E_{rad}(x, z) E_{SP}(z) \, dz \tag{14}$$

The single unknown parameter is the decay length $d_{air}$ of SP in air. The fits are plotted on Fig. 17 for different values of $d_{air}$. For $d_{air} = 0.5$ mm ($\pm 10\%$), the agreement between theory and experiment is very good above $x = 1$ mm, in particular in the far field regime.
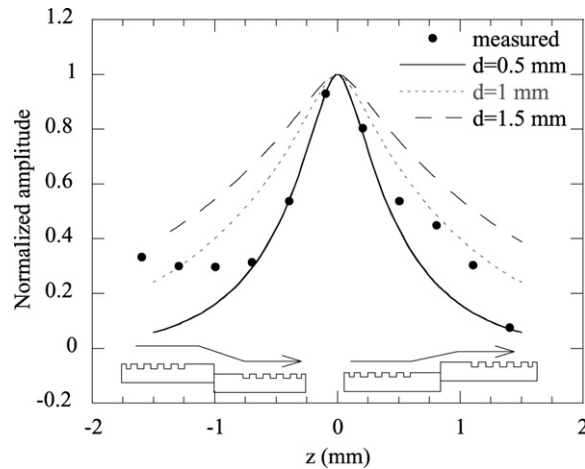
Fig. 18. SP plasmon at 0.475 THz excited at device A and detected at device B versus the elevation $z$ between the two devices. The lines are calculated using a simple scalar Huygens model with the decay length $d_{air}$ of the SP in air as single adjustable parameter.

The decay of the SP field in the $z$ direction, i.e. the part of the field that is evanescent in air, is studied by putting the two devices in contact ($x = 0$) and then varying the difference of elevation $z$ between them. Fig. 18 represents the peak signal at 0.475 THz, detected after the second device, versus $z$. The signal is maximum when the two devices are on the same elevation, i.e. when the SP propagates from one device to the other one without encountering geometrical discontinuity. The signal decreases strongly with the difference of elevation. For weak signals ($|z| > 0.5$ mm), the results are not symmetrical versus $z$: when the first device is higher than the second one, the signal is stronger. We model these results using the coupling efficiency previously defined in (14), which is written here:

$$\eta(x = 0, z) \propto \int_{-\infty}^{+\infty} E_{SP}(0, z') E_{SP}(0, z' + z) \, dz' \tag{15}$$

For small $z$, experimental points are well fitted by the theoretical curves when $d_{air}$ is adjusted to 0.5 mm. This confirms the previous value of $d_{air}$ deduced from the $x$-dependence of the SP-SP coupling (SP jump). For $|z| > 0.5$ mm, the crude overlap-integral model is no more valid. Indeed, it does not take into account scattering effects, and also excitation of SP along the vertical face of the devices.

### 4.8. Epsilon value

From the SP decay length $d_{air}$ in air and the SP propagation attenuation coefficient $\alpha$, we can deduce the value of the dielectric constant $\varepsilon$ of aluminum at 0.475 THz (let us notice that values at other frequencies may be studied by varying the incidence angle using relations (1) and (8)). As we measured $\alpha \approx 0.05$ cm$^{-1}$ and $d_{air} \approx 0.5$ mm, this leads to $Im(\varepsilon) = 900(\pm 50\%)$ [22]. This value differs from data given in the literature [17,18] because of different experimental schemes and conditions, especially the surface state of the metal devices that suffer from oxidation, mechanical roughness or mostly chemical contamination. Recently, Laman and Grischkowsky [28] have shown that the reduced experimental conductivity of several samples of Cu and Al in the THz range can be attributed to a large amount of carrier scattering due to lattice defects within the 100 nm THz skin-depth layer. Here the method of determination is even more sensitive to the surface state, because of the strong interaction of the SP with the surface over a long distance. In the frequency range 0.2–1.5 THz, the real part of epsilon is of the order of $10^3$–$10^5$. Thus, SP experiments are almost insensitive to the exact value of $\varepsilon$ (see Eqs. (2) and (3)), which cannot be determined precisely with this method.

## 5. Conclusion

We have demonstrated that diffraction gratings are efficient couplers to excite SP waves at a metallic surface. Efficient excitation is obtained for an optimized grating groove depth. THz-TDS allows us to separate the different stages

of the coupling process, i.e. the time of excitation of the SP and the rather long time of the decoupling of the propagating SP energy. We have addressed the Bragg phenomenon that occurs when contra-propagating SP are simultaneously excited, and we were able to precisely measure the related frequency bandgap using an original experimental method.

## Acknowledgements

## References

[1] F.C. De Lucia, Spectroscopy in the THz spectral region, in: D.M. Mittleman (Ed.), Sensing with Terahertz Radiation, Springer-Verlag, Berlin, 2003.
[2] D. Bigourd, et al., Multiple component analysis of cigarette smoke using THz spectroscopy, comparison with standard chemical analytical methods, Appl. Phys. B 86 (2006) 579–586.
[3] W.H. Fan, et al., Far-infrared spectroscopic characterization of explosives for security applications using broadband terahertz time-domain spectroscopy, Appl. Spectrosc. 61 (2007) 638.
[4] J.F. Federici, et al., Terahertz imaging using an interferometric array, Proc. SPIE 5790 (2005) 11;
J.F. Federici, et al., THz imaging and sensing for security applications – explosives, weapons, and drugs, Semicond. Sci. Technol. 20 (2005) S266–S280.
[5] G. Mouret, et al., Far-infrared cw difference-frequency generation using vertically integrated and planar low temperature grown GaAs photomixers: application to $H_2S$ rotational spectrum up to 3 THz, Appl. Phys. B 79 (2004) 725–729.
[6] G.C. Schatz, R.P. Van Duyne (Eds.), Electromagnetic Mechanism of Surface-enhanced Spectroscopy, Wiley, New York, 2002.
[7] H. Raether, Surface Plasmons on Smooth and Rough Surfaces and on Gratings, Springer Tracts in Modern Physics, Springer, Berlin, 1986;
R.F. Wallis, G.I. Stegeman (Eds.), Electromagnetic Surface Excitations, Springer Series on Wave Phenomena, Springer, Berlin, 1988.
[8] D.B. Ostrowsky, R. Reinisch (Eds.), Guided Wave Nonlinear Optics, Kluwer Academic Publishers, Dordrecht, 1992.
[9] R. Miles, P. Harrison, D. Lippens (Eds.), Terahertz Sources and Systems Electronics, NATO Science Series II, vol. 27, Kluwer Academic, Dordrecht, 2001.
[10] D. Mittleman (Ed.), Sensing with Terahertz Radiation, Springer Series in Optical Sciences, vol. 85, Springer, Berlin, 2003.
[11] J.W. Lee, et al., Fabry–Pérot effects in THz time-domain spectroscopy of plasmonic band-gap structures, Appl. Phys. Lett. 88 (2006) 071114.
[12] D. Armand et al., Study of the transmission of sub-wavelength metallic grids in the THz frequency range, IEEE J. Selected Topics Quant. Electron. (March 2008), in press.
[13] M. Nazarov, et al., THz surface plasmon jump between two metal edges, Opt. Commun. 277 (2007) 33–39.
[14] J.F. O'Hara, et al., Prism coupling to terahertz surface plasmon polaritons, Opt. Express 13 (2005) 6117.
[15] B. Pradarutti, et al., Plasmonic response in a one-dimensional periodic structure of metallic rods, Appl. Phys. Lett. 87 (2005) 204105;
G. Torosyan, C. Rau, B. Pradarutti, R. Beigang, Generation and propagation of surface plasmons in periodic metallic structures, Appl. Phys. Lett. 85 (2004) 3372.
[16] G. Bogomolov, et al., Nucl. Instrum. Methods Phys. Res. A 543 (2005) 96.
[17] A.D. Rakic, Algorithm for the determination of intrinsic optical constants of metal films: application to aluminum, Appl. Opt. 34 (1995) 4755–4767.
[18] M.A. Ordal, et al., Optical properties of fourteen metals in the infrared and far infrared: Al, Co, Cu, Au, Fe, Pb, Mo, Ni, Pd, Pt, Ag, Ti, V, and W, Appl. Opt. 24 (1985) 4493–4499.
[19] H. Kogelnik, Theory of dielectric waveguides, in: T. Tamir (Ed.), Integrated Optics, Springer-Verlag, New York, 1995.
[20] R. Reinisch, et al., Gratings and prisms couplers: radiation pattern and $m$-line, Opt. Commun. 120 (1995) 121–128.
[21] D.D. Maystre, The integral method, in: R. Petitt (Ed.), Electromagnetic Theory of Gratings, Springer-Verlag, Berlin, 1980, pp. 63–100.
[22] M. Nazarov, et al., THz surface plasmon jump between two metal edges, Opt. Commun. 277 (2007) 33–39.
[23] L.S. Mukina, et al., Propagation of THz plasmon pulse on corrugated and flat metal surface, Surf. Sci. 600 (2006) 4771–4776.
[24] J.-F. Roux, et al., Grating-assisted coupling of terahertz temporal waves into a dielectric waveguide studied by terahertz time-domain spectroscopy, Appl. Opt. 41 (2002) 6507–6513.
[25] F. Aquistapace, et al., Photo-variation of grating-assisted coupling of THz waves into a silicon waveguide, J. Appl. Phys. 94 (2003) 7888–7891.
[26] T.-I. Jeon, D. Grischkowsky, THz Zenneck surface wave (THz surface plasmon) propagation on a metal sheet, Appl. Phys. Lett. 88 (2006) 061113.
[27] M.M. Nazarov, et al., Excitation and propagation of surface electromagnetic waves studied by terahertz spectrochronography, Laser Phys. Lett. 2 (2005) 471–475.
[28] N. Laman, D. Grischkowsky, Reduced conductivity in the terahertz skin-depth layer of metals, Appl. Phys. Lett. 90 (2007) 122115.